Journal of Materials Chemistry C

Temperature–insensitive high piezoelectricity in (Bi0.5K0.5)TiO3–PbTiO3–PbZrO3 ternary system

Journal:	*Journal of Materials Chemistry C*
Manuscript ID	TC-ART-06-2024-002553.R1
Article Type:	Paper
Date Submitted by the Author:	30-Jul-2024
Complete List of Authors:	Yan, Shengjie; University of Science and Technology Beijing Di, Siyun; University of Science and Technology Beijing Yang, Mingyu; University of Science and Technology Beijing Zhang, Yueyun; University of Science and Technology Beijing Sun, Zheng; University of Science and Technology Beijing Liu, Hui; University of Science and Technology Beijing

Temperature–insensitive high piezoelectricity in $(Bi_{0.5}K_{0.5})TiO_3$–$PbTiO_3$–$PbZrO_3$ ternary system

Shengjie Yan[1,#], Siyun Di[1,#], Mingyu Yang[1,#], Yueyun Zhang[1,*], Zheng Sun[1], and Hui Liu[1,*]

[1]*Beijing Advanced Innovation Center for Materials Genome Engineering, and School of Mathematics and Physics, University of Science and Technology Beijing, Beijing 100083, China*

[#] *Shengjie Yan, Siyun Di, and Mingyu Yang contribute equally to this work.*

**Corresponding authors: zyy_ustb@163.com and huiliu@ustb.edu.cn*

Abstract

Piezoelectric actuators operating in harsh environments require piezoelectric ceramics with high and temperature–insensitive piezoelectric responses, which poses a significant challenge due to the inverse correlation between the piezoelectric d_{33} and the Curie temperature (T_C). In this study, a novel ternary system of $Bi_{0.5}K_{0.5}TiO_3$–$PbTiO_3$–$PbZrO_3$ (BKT–PT–PZ) is explored for high–temperature piezoelectric materials by considering the local structural heterogeneity and tolerance factor. The ferroelectric, piezoelectric, dielectric, phase structure and temperature stability of xBKT–0.32PT–(0.68–x)PZ ($0.13 \leq x \leq 0.17$) are systematically studied. The optimal piezoelectric d_{33} value exceeding 350 pC/N, maintained up to 320 ℃, is achieved at x = 0.15. Significantly, a large strain of 0.24% is obtained at 4 kV/mm, corresponding to a piezoelectric strain response of 682 pm/V. The strain variation within 20% observed at the range of 25-275 ℃ demonstrates excellent temperature stability. The *in situ* high–energy synchrotron X–ray diffraction (SXRD) and piezoresponse force microscope (PFM) indicate that the lattice strain and stable nanosized domains till to 200 ℃ contribute to the high piezoelectricity and excellent temperature–insensitive properties, respectively. This outstanding feature positions it as a strong candidate for the next generation of piezoelectric actuators.

1. Introduction

Piezoelectric ceramics play a critical role in converting electrical into mechanical energy through electromechanical coupling, offering diverse applications as actuators, sensors, and transducers. [1, 2] Piezoelectric actuators are extensively utilized in various fields such as fuel injector systems and automobile motors.[3, 4] The aerospace and automotive industries stand out as significant sectors where piezoelectric actuators are widely integrated. These actuators are expected to demonstrate exceptional precision, rapid response times, low driving voltage demands, and superior temperature stability.[3, 5] One of the major challenges faced by actuator applications is their operation in elevated temperature conditions. From a material perspective, there is a pressing need to develop piezoelectric materials with both high piezoelectricity and excellent thermal stability.[6]

Among all piezoceramics, the $Pb(Zr,Ti)O_3$ (PZT)–derived systems still hold a dominant position in the market due to its exceptional piezoelectric properties, robust durability, and low manufacturing cost. [7, 8] Consequently, significant efforts have made to improve its piezoelectric properties for high–temperature applications. However, achieving both high piezoelectric response and good temperature stability simultaneously remain a challenge. For instance, by incorporating relaxor end–number such as $Pb(Ni_{1/3}Nb_{2/3})O_3$ or $Pb(Mg_{1/3}Nb_{2/3})O_3$ to flatten the free energy profile can significantly enhance the piezoelectric strain but may compromise temperature stability due to the ferroelectric phase transitions. [9-12] Conversely, substituting end–numbers with high Curie temperature (T_C) can enhance the thermal stability but may lead to a reduction in piezoelectricity. A trade-off behavior exists between piezoelectricity and temperature stability. [13]

Recent studies have shown that a promising approach to achieving high piezoelectric response and excellent thermal stability involves introducing an end member with a high T_C and substituting heterovalent ions to form local structural heterogeneity simultaneously. For instance, the Sm–modified $Pb(In_{1/2}Nb_{1/2})O_3$–$PbZrO_3$–$PbTiO_3$ (PIN-PZ-PT) exhibits a piezoelectric response of 945 pm/V, with minimal variation of 7% up to 310 °C. [14] The lead–free $(Bi_{0.5}K_{0.5})TiO_3$ (BKT) end–

number systems usually exhibit a high T_C (about 400 °C). [15-17] The combination of heterovalent ions Bi^{3+} (1.34 Å) and K^+ (1.64 Å) in *A*–site results in the similar size to Pb^{2+} (1.49 Å). Given these factors, it is hypothesized that the introduce of BKT can have a beneficial impact on enhancing the piezoelectric properties of PZT.

In this study, a novel $Bi_{0.5}K_{0.5}TiO_3$–$PbTiO_3$–$PbZrO_3$ (BKT–PT–PZ) ternary system is investigated with detailed phase structure, electric properties, temperature stability and domain structure. An optimal high d_{33} of 426 pC/N and high T_C of 300 ℃ are achieved in 0.15BKT–0.32PT–0.53PZ ceramic. Specifically, a high strain of 0.24% (d^*_{33} = 682 pm/V) at room temperature and a variation of less than 20% with excellent temperature–insensitive ranging from 25-275 °C are observed. The *in situ* high–energy SXRD and temperature–dependent domain structure experiments provide insights into the contribution to both excellent piezoelectric properties and temperature stability.

2. Experimental procedures and characterization methods

A modified solid–state method is utilized to synthesize *x*BKT–0.32PT–(0.68–*x*)PZ ($0.13 \leq x \leq 0.17$) ceramics using Bi_2O_3, PbO, K_2CO_3, ZrO_2, and TiO_2 as raw materials. The raw materials are weighed according to the stoichiometric ratios, with an additional 1–2% added to account for the high–temperature volatility of certain substances like Pb, Bi, and K. The raw materials are homogeneously mixed and calcined at 850 ℃ for 2 hours to form a perovskite structure. The calcined powder added with polyvinyl alcohol (PVA) is pressed into green disks with a diameter of 10 mm. After the removing of PVA at 550 ℃ for 2 hours, the green disks are followed by sintered at 1150–1250 ℃ for 2 hours to get dense ceramics.

The phase structure at room temperature is identified using X–ray powder diffraction (XRD, PANalytical, X'Pert PRO, Netherlands) with Cu Kα radiation. The grain morphology is examined via scanning electron microscopy (SEM), and SEM images are analyzed using Image J software to calculate the average grain size. The microscopic domain configurations of an unpoled ceramic are observed using a PFM

along with an AFM system (Asylum Research, MFP–3D, USA). *In situ* high–energy SXRD data is collected at 11–ID–C beamline at the Advanced Photon Source with a transmission mode (the wavelength is 0.1173 Å).

The d_{33} values are measured using a quasi–static d_{33} meter (Institute of Acoustics, Chinese Academy of Sciences, ZJ–6A) with polarized ceramics under 4 kV/mm for 15 minutes. Dielectric constant and loss are tested by an impedance analyzer (Agilent E4980A), operating within a frequency range of 0.1–1000 kHz, a test temperature range of 25–500 °C, and a ramp rate of 3 °C/min. A ferroelectric analyzer (aix ACCT, TF Analyzer 1000, Aachen, Germany) is employed to measure the ferroelectric hysteresis (*P–E*), strain curves (*S–E*) at room temperature with a test frequency of 1–5 Hz.

3. Results and discussion

3.1 Phase structure and microscopic morphologies

It is widely recognized that the high piezoelectricity of perovskite–type ferroelectrics typically occurs at the phase boundary and is characterized by a tolerance factor (*t*) near 1 with smaller lattice distortion.[18] Therefore, the BKT–PT–PZ ternary system is explored to figure out the optimal d_{33} with the help of *t* in the phase diagram (Fig. 1(a)). It is evident that a series of compositions display a high d_{33} value exceeding 400 pC/N within the composition region where the tolerance factor *t* is 0.9881. Notably, an optimal d_{33} of 426 pC/N is achieved in 0.15BKT–0.32PT–0.53PZ, which is superior to other chemical–modified PZT ceramics, such as the PZT–4 (289 pC/N), PZT–5 (374 pC/N), [19] (K,Na,Li)NbO_3–PZT (363 pC/N). [20] A series of *x*BKT–0.32PT–(0.68–*x*)PZ ($0.13 \le x \le 0.17$) composition is studied in detail. As depicted in the XRD pattern (Fig. 1(b)), all samples demonstrate a single perovskite–type structure without the presence of any secondary phases, suggesting that Bi^{3+} and K^{+} ions are incorporated into the perovskite lattice matrix, leading to a solid solution with uniform composition. As the BKT content increases from 0.13 to 0.17, the symmetrical (200) peak gradually transforms into a broad and split peak, suggesting that the crystal structure is evolving

from the rhombohedral (*R*) phase towards the rhombohedral–tetragonal (*R*–*T*) phase coexistence. Near $x = 0.15$, the crystal structure demonstrates a morphotropic phase boundary (MPB), where the *R* and *T* phases reach an equivalent energy state with enhanced polarizability. [8] As a result, the piezoelectric properties reach the peak value.

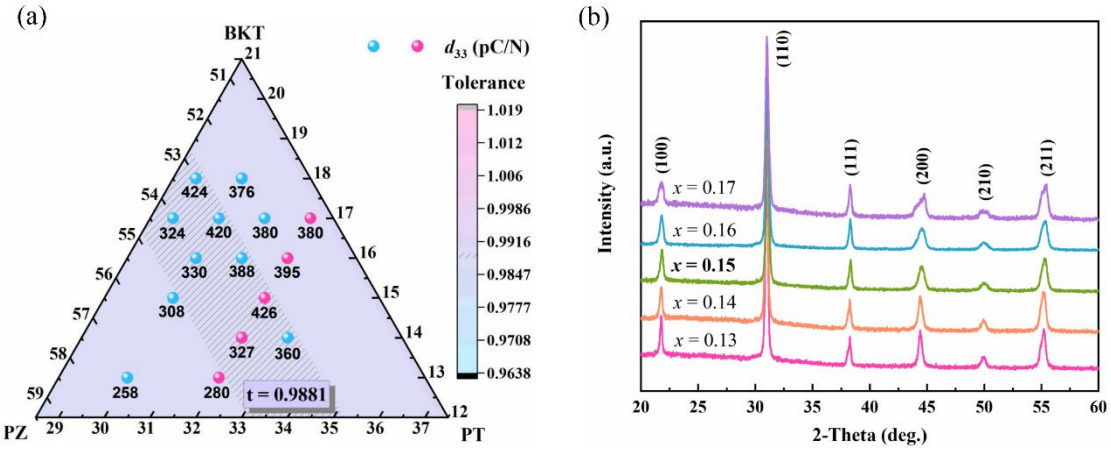

Fig. 1(a). The phase diagram associated with d_{33} and *t* of BKT–PT–PZ ternary system, (b) XRD patterns of *x*BKT–0.32PT–(0.68–*x*)PZ ($0.13 \leq x \leq 0.17$) ceramics.

The microstructure and grain size are characterized through SEM analysis (Fig. 2(a–c)). The ceramic grains are neatly arranged, uniform in size and distinct grain boundaries, showing a high–density structure with no discernible pores. The observation suggests that the sample underwent complete reaction at the corresponding sintering temperature. Fig. 2(d–f)) shows that there is no obvious difference in the average grain size of three samples (~1 μm), which is consistent with PZT-based (1.34 μm) and BKT-based systems (0.99 μm).[21, 22] This grain size of 1 μm is a critical size in lead–free systems such as $BaTiO_3$–based ceramic, which tends to produce a high piezoelectric d_{33}. [23-25]

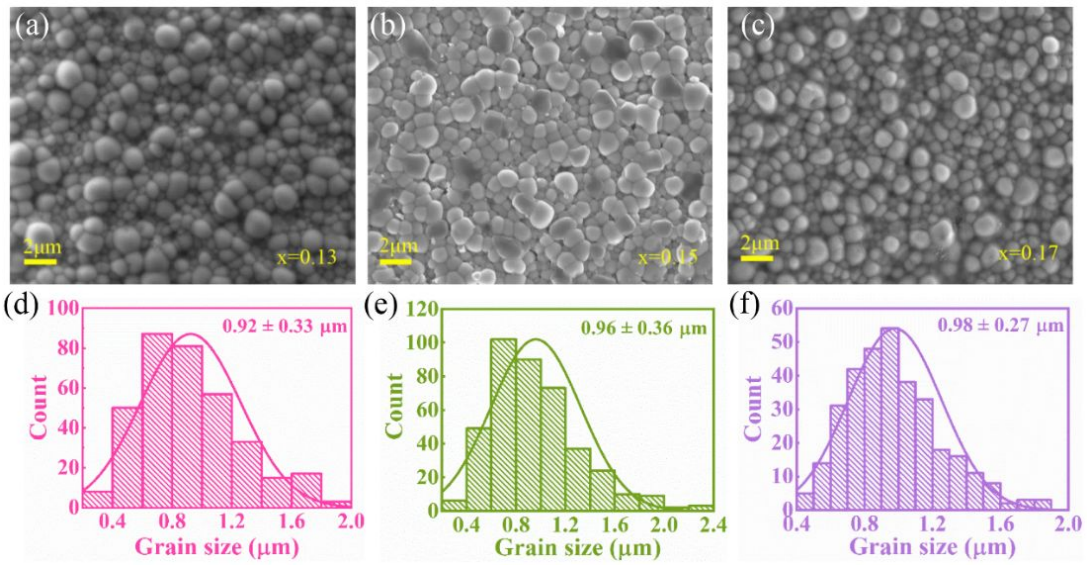

Fig. 2. (a–c) SEM micrographs, and (d–f) corresponding grain size distribution of *x*BKT–0.32PT–(0.68–*x*)PZ (*x* = 0.13, 0.15, and 0.17) ceramics.

3.2 Ferroelectric, piezoelectric and dielectric properties

The ferroelectric polarization behavior of *x*BKT–0.32PT–(0.68–*x*)PZ ($0.13 \le x \le 0.17$) ceramics are evaluated under a bipolar *E* of 4 kV/mm (Fig. 3(a–b)). All compositions show typical ferroelectric *P*–*E* loops and strain curves. The evolution of electrical parameters including remnant polarization (P_r), coercive field (E_C), and total strain (S_{total}) are extracted in Fig. 3(c). The P_r and E_C show a opposite monotonicity with increasing BKT content. Near PZT, the components exhibit higher P_r at $x \le 0.14$. The E_C is closely linked to the lattice distortion. A greater lattice distortion is unfavorable for domain switching and typically corresponds to a higher E_C. Due to pure tetragonal phase structure with a large c/a ratio of 1.02 in BKT, [26] the domain is difficult to switch under the influence of an electric field, resulting in a higher E_C value in compositions which is rich in BKT ($x \ge 0.16$). Specially, the MPB composition of x = 0.15 exhibits a relatively large P_r of 38 μC/cm^2 and E_C of 1.61 kV/mm. The total strain (S_{total}) is determined by the sum of positive and negative peak values. At x = 0.15, the S_{total} reaches a maximum value of 0.54%, which is much higher than other PZT–based and BKT–based systems.[17, 27-29] The 0.15BKT–0.32PT–0.53PZ show optimal

performance and great potential for applications in piezoelectric actuators.

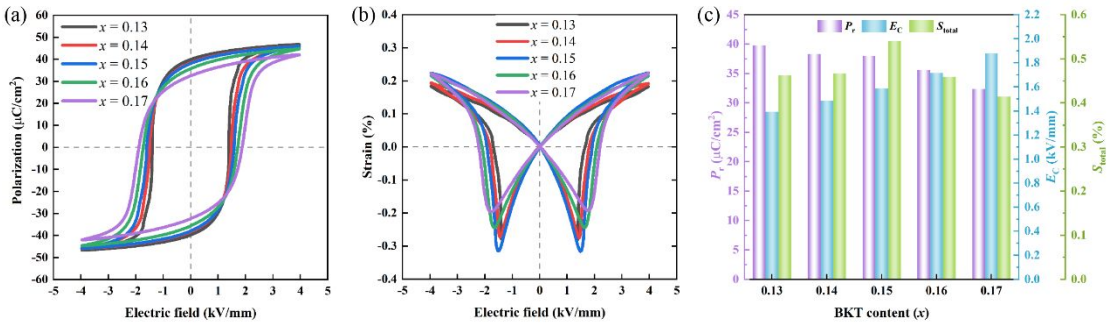

Fig. 3. (a) *P*–*E*, (b) *S*–*E* curves, and (c) extracted P_r, E_C and S_{total} values of 0.32PT–*x*BKT–(0.68–*x*)PZ ($0.13 \leq x \leq 0.17$) ceramic at 4 kV/mm.

Fig. 4(a) presents the unipolar strain curves of *x*BKT–0.32PT–(0.68–*x*)PZ ($0.13 \leq x \leq 0.17$) ceramics under various electric field (2~4 kV/mm) at room temperature. It can be seen that the unipolar strain become slenderer when the electric field is enhanced. The change of unipolar strain is consistent with the trend of the S_{total} in Fig. 3(c) with the increase of BKT content. Notably, the peak strain value of 0.24% is achieved in the $x = 0.15$ composition at 4 kV/mm. The d_{33}^* (S_{max}/E_{max}) of *x*BKT–0.32PT–(0.68–*x*)PZ ceramics under different electric field is calculated in Fig. 4(b). When $x \leq 0.14$, d_{33}^* decreases monotonically with *E*. While $x \geq 0.15$, this relationship changes and d_{33}^* reaches its maximum value at the intermediate *E* of 3 kV/mm. As the electric field increases from 2 kV/mm to 4kV/mm, the field–induced strains gradually increases but d_{33}^* decreases slightly. This phenomenon is also found in other lead–based systems, which may be due to the clamping of partial domains under high electric fields and the inability to switch.[30, 31] The d_{33}^* value shows a trend of first increasing and then decreasing with increasing BKT content. At MPB composition ($x = 0.15$), the ceramic under different electric field exhibits high d_{33}^* of 665, 682 and 601 pm/V respectively. Compared with other compositions, 0.15BKT–0.32PT–0.53PZ ceramic shows excellent electrical properties of 682 pm/V, which is exceed lead-based $Pb(Yb_{0.5}Nb_{0.5})O_3$–$PbHfO_3$–$PbTiO_3$ (620 pm/V) and lead-free $(Bi_{0.5}K_{0.5})TiO_3$–$Bi(Mg_{0.5}Ti_{0.5})O_3$ (314 pm/V) systems. [29, 31]

Temperature-dependent dielectric spectrum of poled *x*BKT–0.32PT–(0.68–*x*)PZ ceramics at different frequencies are measured (Fig. 4(c)). The dielectric maximum of different composition decreases with the increase of frequency, and gradually moves to the high temperature, exhibiting the frequency dispersion and diffuse phase transition behavior. [32-34] All compositions ($0.13 \leq x \leq 0.17$) exhibit a high T_C over 300 °C, implying prominent temperature stability in this system. Notably, T_C reaches maximum value of 308 ℃ at MPB composition, while is inferior to the common high-temperature $BiScO_3$-$PbTiO_3$ and $Pb(In_{1/2}Nb_{1/2})O_3$-$PbTiO_3$ systems with a T_C of 450 °C and 312 °C, respectively, but exceeding Sm^{3+}doped $Pb(Mg_{1/3}Nb_{2/3})O_3$–$PbZrO_3$–$PbTiO_3$ (Sm–PMN–PZ–PT) system of 242 °C.[35-37] Moreover, all compositions show a small dielectric loss (< 0.045) under the electric field. Studies have shown that the piezoelectric properties are directly proportional to the dielectric constant and ferroelectric polarization, which can be described as $d_{33} \propto \varepsilon_r \times P_r$ (ε_r is the dielectric constant at room temperature). [38, 39] The larger dielectric properties and polarization are beneficial to obtain a higher d_{33}. With the increase of BKT content, piezoelectric d_{33} and $\varepsilon_r \times P_r$ present the coincident trend, and both reached the optimal value at $x = 0.15$ in Fig. 4(d).

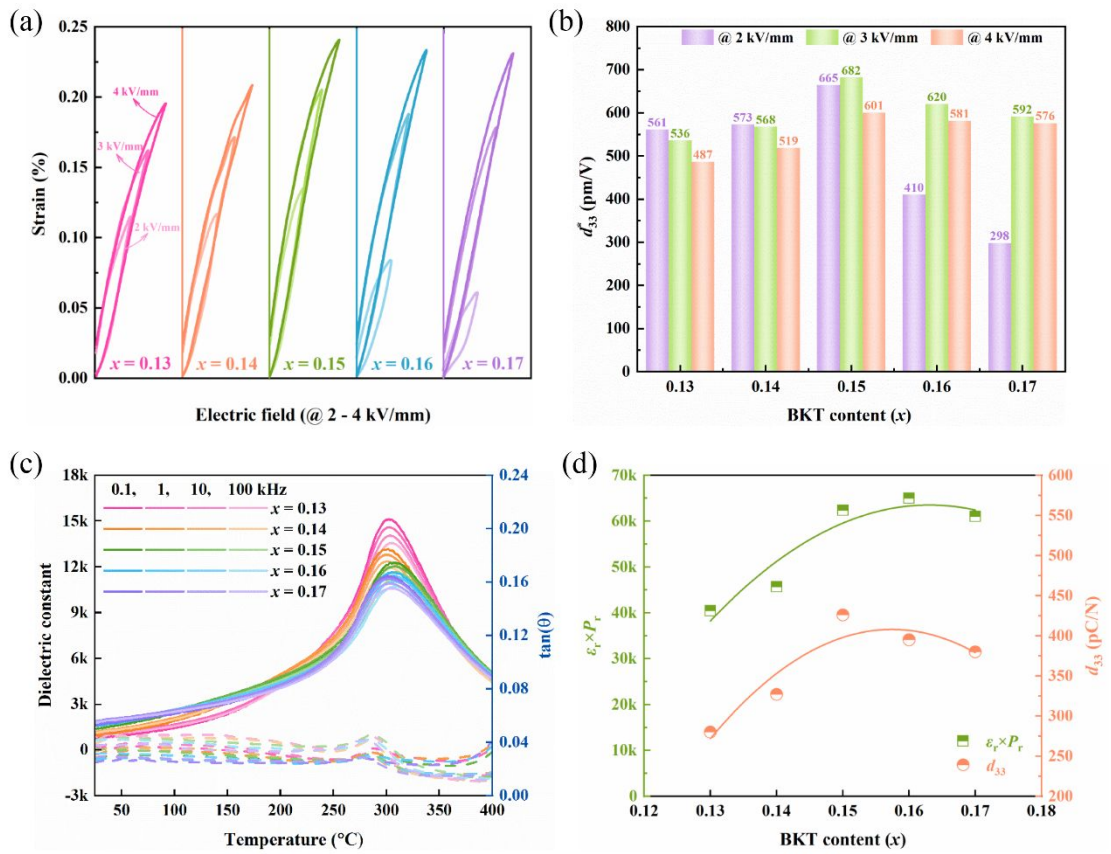

Fig. 4. (a) Unipolar strain curves under different electric field at room temperature, (b) d_{33}^{*}, (c) Temperature–dependent of dielectric spectrum at 0.1,1,10 and 100 kHz. (d) The relationship between $\varepsilon_r \times P_r$ and d_{33} as a function of BKT content.

3.3 Temperature stability

For piezoelectric actuator application, the temperature stability is important to the operation at high temperature. The *in-situ* d_{33} values *vs* temperature of *x*BKT–0.32PT–(0.68–*x*)PZ (x = 0.14, 0.15, and 0.17) are shown in Fig. 5. With the temperature increasing, the d_{33} value gradually increases, and drops significantly around T_C, which is consistent with the temperature–dependent dielectric behavior (Fig. 4(c)). The ceramics transforms from ferroelectric to paraelectric phase near T_C, and the internal polar dipole returns to a disordered state, which leads to the deterioration of piezoelectric properties. At x = 0.15, the *in-situ* d_{33} reaches largest value of 488 pC/N at 150 °C, and gradually decreases to 350 pC/N at T_C due to the depolarization behavior.[38, 40] High d_{33} (> 365 pC/N) is maintained in the range of 25-300 °C. The

sensitivity coefficient (η) is used to describe the temperature stability of the d_{33} value, which can be calculated as the following formula:

$$\eta = \frac{(d_{33})_T - (d_{33})_{200°C}}{(d_{33})_{200°C}} \times 100\% \quad (1)$$

Where $(d_{33})_T$ and $(d_{33})_{200°C}$ are the piezoelectric coefficient at the measurement temperature T and 200 °C, respectively. [38] The insensitive temperature ΔT of 0.32PT–0.15BKT–0.53PZ is 236 °C when the η fluctuates within 15 %. Moreover, other components also have a wide insensitive temperature ΔT in the range of η floating ±15%, which is 172 °C (x = 0.14) and 258 °C (x = 0.17). It suggests that the incorporation of BKT expands temperature-insensitive range and greatly improves its potential in practical application.

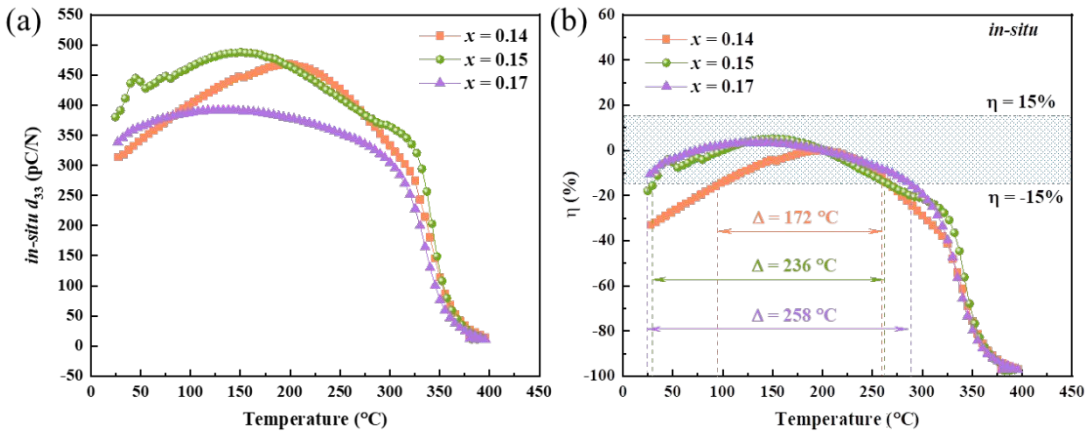

Fig. 5. (a) *In-situ* measurement of piezoelectric d_{33}, and (b) sensitivity coefficient η as a function of temperature for 0.32PT–xBKT–(0.68–x) PZ (x = 0.13, 0.15, and 0.17) ceramics.

To further evaluate the temperature stability of the sample at MPB (x = 0.15), temperature–dependent unipolar strains at 1 kV/mm and 4 kV/mm are measured (Fig. 6(a–b)). It can be seen that when the temperature is lower than 200 °C, the strain increases slightly with increasing temperature, while it begins to decrease when the temperature is higher than 200 °C, which is consistent with the change of *in-situ* d_{33} in Fig.5(a). The 0.32PT–0.15BKT–0.53PZ ceramic shows a high strain value (> 0.23%) at 4 kV/mm, and the maximum value can reach 0.29%. The strain variation from 50℃

to 275 °C is 27% (1 kV/mm) and 20% (4 kV/mm), which is comparable with temperature-insensitive Sm–modified 0.15PMN–0.43PZ–0.42PT (20%) and 0.25PIN–0.325PZ–0.425PT (25%) systems.[14, 41] Notably, the unipolar strains gradually turn thinner with a low hysteresis under the induction of high electric field and high temperature, which is related to the irreversible domain wall motion. [42, 43] The small hysteresis of strain and good temperature stability are conducive to the application of high-precision actuators in high temperature environments.[18] As shown in Fig. 4, the unipolar strain and the d_{33}^* are inseparable under the electric field. Meanwhile, temperature-insensitive of piezoelectric d_{33}^* in diffident electric field are also calculated in Fig. 6(c). The MPB composition of 0.32PT–0.15BKT–0.53PZ maintains a high d_{33}^*(>600 pm/V) in the range of 25–275 ℃ at 1-4 kV/mm. Among them, it shows ultrahigh d_{33}^* of 943 pm/V at 175℃, which is superior to Sm-doped 0.15PMN–0.42PZ–0.43PT and $0.48Pb(Mg_{1/3}Nb_{2/3})O_3$–$0.1Pb(Fe_{1/2}Nb_{1/2})O_3$–$0.1PbZrO_3$–$0.32PbTiO_3$ in the same condition.[3, 44] On the whole, the above results confirm that 0.32PT–0.15BKT–0.53PZ ceramic is equipped with both excellent electrical and thermal properties and it is expected to applied in a new generation of high temperature insensitive piezoelectric actuator.

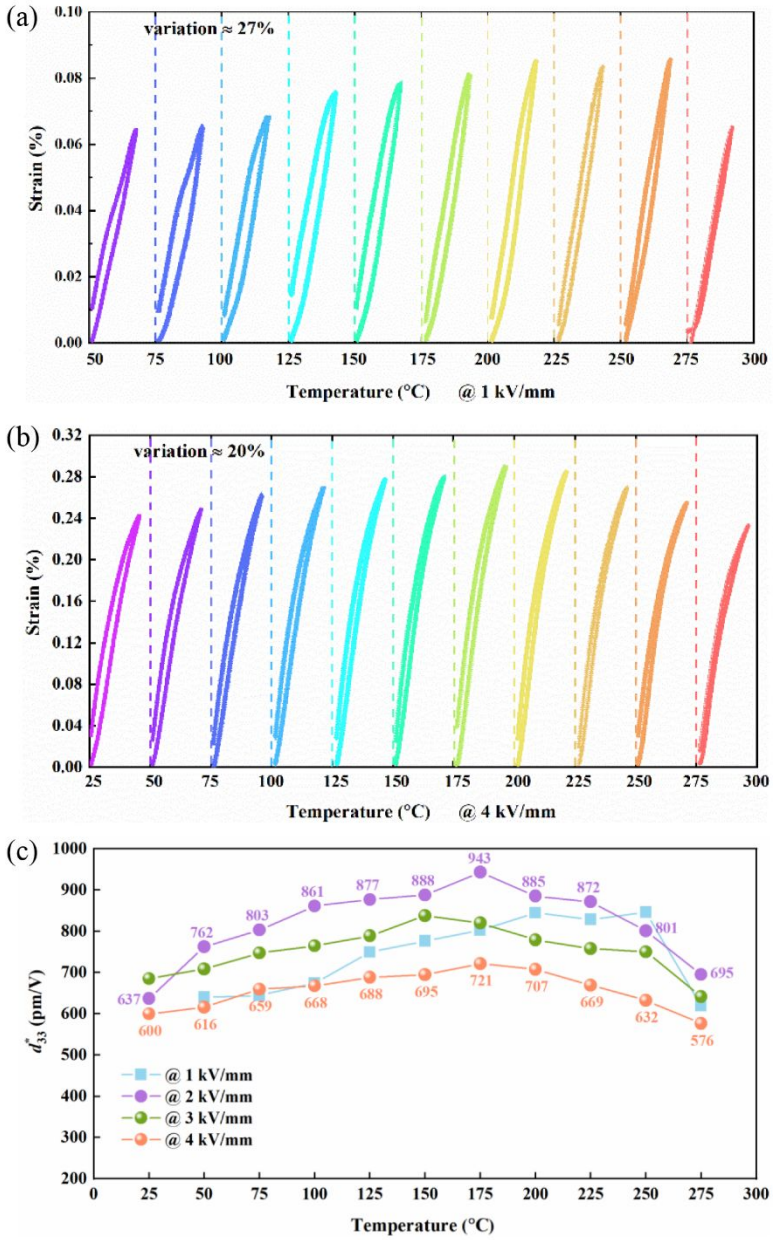

Fig. 6. Temperature–dependent unipolar strain of 0.15BKT–0.32PT–0.53PZ ceramic measured at (a) 1kV/mm, and (b) 4 kV/mm. (c) Temperature stability of d^*_{33}.

As mentioned above, the 0.15BKT–0.32PT–0.53PZ composition exhibits the best piezoelectric properties. In order to explore the source of high piezoelectricity, *in–situ* SXRD technology is used to study the crystal structure under *in–situ* electric field. As shown in Fig. 7(a), the peak position and peak intensity of $(111)_p$ and $(200)_p$ profiles change regularly during the process of loading and unloading electric field, indicating that a large lattice strain is generated in this composition, which provides the intrinsic

contribution to piezoelectric properties.[45, 46] The $(111)_p$ and $(200)_p$ peaks maintain a single broad profile without splitting under the disturbance of the electric field, indicating that the composition exhibits a pseudo–cubic phase structure (Fig. 7(b)). Such structure is commonly found in lead-based relaxor systems and prone to induce a high piezoelectric response.[30, 47, 48]

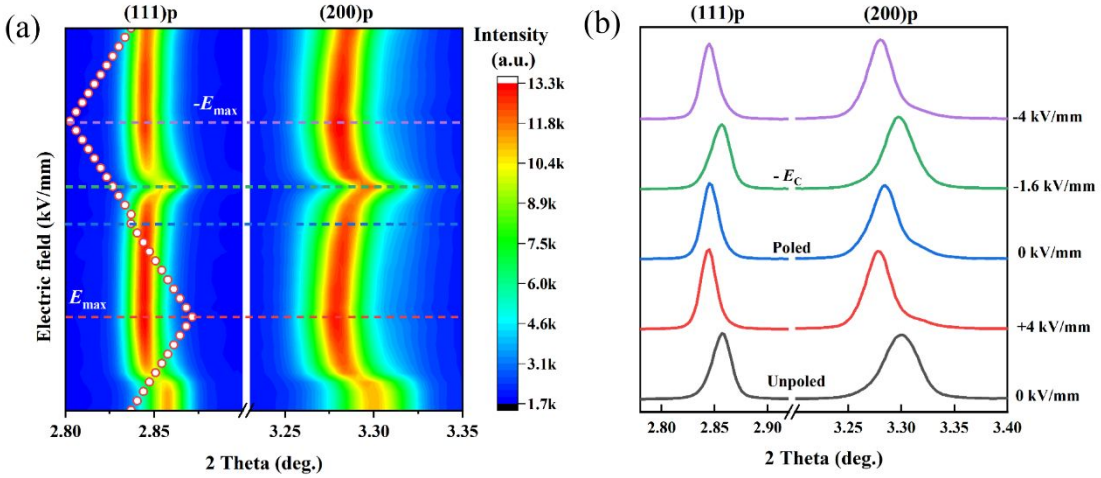

Fig. 7. (a) The $(111)_p$ and $(200)_p$ profiles as the function of *in–situ* electric field, and (b) the $(111)_p$ and $(200)_p$ under specific electric fields at 0° sector of 0.15BKT–0.32PT–0.53PZ.

It is well known that microscopic domain structure is closely related to piezoelectric properties as an external contribution.[6, 30] In order to explore the relationship between enhanced temperature–insensitive piezoelectric properties and domain structure, temperature–dependent *in–situ* PFM is carried out in Fig. 8. Out of plane amplitude and phase images from 25℃ to 200 ℃ are shown in Fig. 8(a_1–e_2). At room temperature, irregular island and branch–shaped domains of several hundred nanometers are present in 0.15BKT–0.32PT–0.53PZ ceramic, and such domain structures are also observed in temperature–insensitive $BiScO_3$–$PbTiO_3$–$Bi(Zn_{1/2}T_{i1/2})O_3$ (BS–PT–BZT) piezoelectric system.[6] Nanoscale domains respond very quickly to electric fields and are prone to produce high piezoelectric properties of 350 pC/N in this system and of 520 pC/N in BS–PT–BZT system.[6, 47] When the increase of

temperature, the number of nanosized domains gradually increases. When the temperature reaches 150 ℃, a large area of extremely tiny size domains appears in the ceramic. At this time, the electrical domains still keep a high degree of activity, inducing the high piezoelectric response of this component to exceed 800 pm/V and reach a peak of 943 pm/V at 175℃ (Fig.6c). The piezoelectric d_{33} in Fig. 5 also show the same trend. Eliminating the influence of surface morphology in Fig. 8(a_3–e_3), PFM confirmed that 0.15BKT–0.32PT–0.53PZ ceramic has always maintained this nano–sized domain in the range of room temperature to 200 ℃, which explains both the excellent temperature stability and high piezoelectric properties in this system.

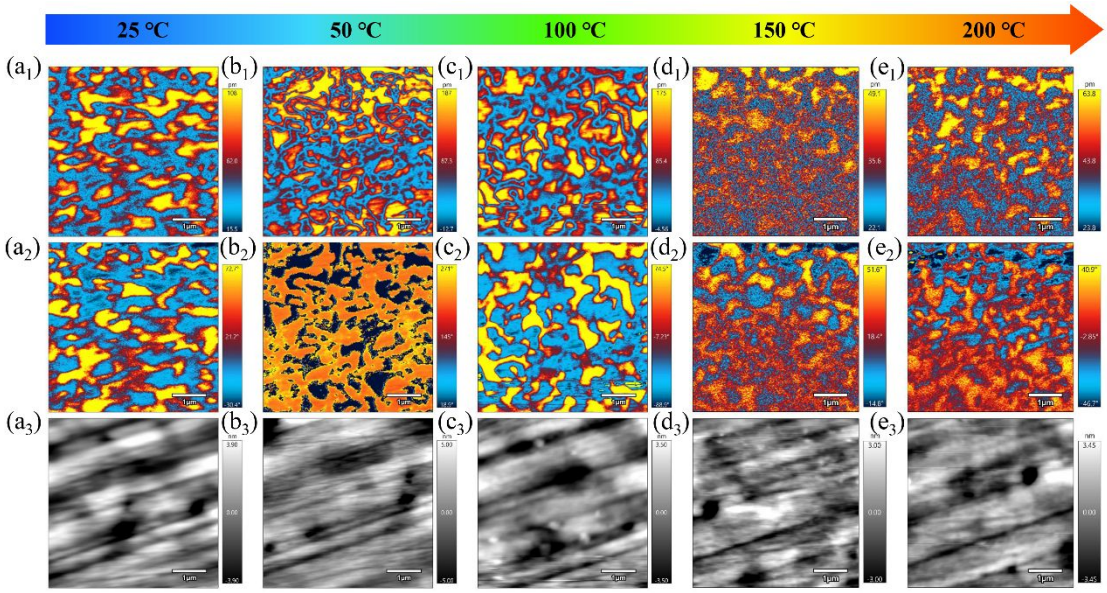

Fig. 8. *In situ* temperature–dependent PFM characterization in 0.15BKT–0.32PT–0.53PZ ceramic: (a_1–e_1) out of plane amplitude, (a_2–e_2) phase images and (a_3–e_3) surface topography as a function of temperature: 25 ℃, 50 ℃, 100 ℃, 150 ℃ and 200 ℃. The scanning area is 5 × 5 μm.

4. Conclusions

In this work, the phase structure, related electrical properties and microscopic domain structure of *x*BKT–0.32PT–(0.68–*x*)PZ system are systematically studied. A high d_{33} of 426 pC/N and high T_C of 300 ℃ are simultaneously realized in the MPB

composition (x = 0.15). Importantly, a large strain of 0.29% and ultrahigh d_{33}^* of 943 pm/V are carried out at the range of 25-275 ℃ with an outstanding temperature stability of strain variation within 20%. The *in-situ* SXRD data show that the MPB composition exhibits a large lattice strain under the electric field. Temperature-dependent PFM confirms that stable nanosized domain structure at 25-200 ℃ supports good temperature-insensitive high piezoelectricity in this system. The above excellent properties make it a strong competitor for the next generation of piezoelectric ceramic actuators.

Conflicts of interest

The authors declare no conflicts of interest.

Acknowledgments

This work was supported by the National Natural Science Foundation of China (22075014) and the Fundamental Research Funds for the Central Universities, China (06500162). This research used resources of the Advanced Photon Source; a US Department of Energy (DOE) Office of Science User Facility operated for the DOE Office of Science by Argonne National Laboratory under contract no. DE-AC02-06CH11357.

References

1. P. K. Panda, B. Sahoo and T. S. Thejas, *Sensors International*, 2023, **4**, 100226.
2. J. F. Tressler, S. Alkoy and R. E. Newnham, *J. Electroceram.*, 1998, **2**, 257-272.
3. Q. Guo, X. Meng, F. Li, F. Xia, P. Wang, X. Gao, J. Wu, H. Sun, H. Hao, H. Liu and S. Zhang, *Acta Mater.*, 2021, **211**, 116871.
4. C. A. Randall, A. Kelnberger, G. Y. Yang, R. E. Eitel and T. R. Shrout, *J. Electroceram.*, 2005, **14**, 177-191.
5. X. Gao, J. Yang, J. Wu, X. Xin, Z. Li, X. Yuan, X. Shen and S. Dong, *Adv. Mater. Technol.*, 2020, **5**, 1900716.
6. Z. Liu, C. Zhao, J.-F. Li, K. Wang and J. Wu, *J. Mater. Chem. C*, 2018, **6**, 456-463.
7. P. K. Panda and B. Sahoo, *Ferroelectrics,* 2015, **474**, 128-143.
8. T. R. Shrout and S. J. Zhang, *J. Electroceram.*, 2007, **19**, 113-126.

9. Q. Guo, F. Li, F. Xia, X. Gao, P. Wang, H. Hao, H. Sun, H. Liu and S. Zhang, *ACS Appl. Mater. Interfaces*, 2019, **11**, 43359-43367.
10. K. H. Yoon and H. R. Lee, *J. Appl. Phys.*, 2001, **89**, 3915-3919.
11. L. Bian, X. Qi, K. Li, J. Fan, Z. Li, E. Sun, B. Yang, S. Dong and W. Cao, *J. Eur. Ceram. Soc.*, 2021, **41**, 6983-6990.
12. H. Wang, F. Zhang, Y. Chen, C. Huang, X. Wang, X. Wu, Y. Chen, Y. Xu, S. Guan, J. Zhu, Q. Chen and J. Xing, *Ceram. Int.*, 2021, **47**, 12284-12291.
13. S.-E. Park and T. R. Shrout, *J. Appl. Phys.*, 1997, **82**, 1804-1811.
14. P. Wang, Q. Guo, F. Li, F. Xia, H. Hao, H. Sun, H. Liu and S. Zhang, *J. Eur. Ceram. Soc.*, 2022, **42**, 3848-3856.
15. Z. Pan, Q. Wang, J. Chen, C. Liu, L. Fan, L. Liu, L. Fang and X. Xing, *J. Am. Ceram. Soc.*, 2015, **98**, 104-108.
16. A. Prasatkhetragarn, B. Yotburut, N. Triamnak, R. Yimnirun and D. P. Cann, *Ceram. Int.*, 2012, **38**, 827-830.
17. A. Zeb, D. A. Hall and S. J. Milne, J. Mater. *Sci.-Mater. Electron.*, 2015, **26**, 9516-9521.
18. S. Sun, Y. Liu, Y. Zhang, L. Wang, S. Deng, Y. Ren, H. Qi, H. Liu and J. Chen, *J. Eur. Ceram. Soc.*, 2022, **42**, 112-118.
19. C. A. Randall, N. Kim, J.-P. Kucera, W. Cao and T. R. Shrout, *J. Am. Ceram. Soc.*, 1998, **81**, 677-688.
20. Q. Yin, S. Yuan, Q. Dong and C. Tian, *J. Am. Ceram. Soc.*, 2010, **93**, 167-170.
21. W. Liu, F. Zhang, T. Zheng, H. Li, Y. Ding, X. Lv, Z. Gao and J. Wu, *J Mater Sci Technol,* 2024, **192**, 19-27.
22. X. Liu, T. Ai, Y. Zheng, X. Chen, Q. Li, Q. Qiu, Y. Zheng, Y. Zhou, H. Song, K. Yu, C. Song, H. Zhang, Y. Yan and G. Liu, *Ceram. Int.,* 2024, **50**, 26193-26204.
23. Y.-X. Liu, Z. Li, H.-C. Thong, J.-T. Lu, J.-F. Li, W. Gong and K. Wang, *Acta Phys. Sin.*, 2020, **69**.
24. X. Liu, S. Xue, F. Wang, J. Zhai and B. Shen, *Acta Mater.*, 2019, **164**, 12-24.
25. Y. Huan, X. Wang, J. Fang and L. Li, J. *Exp. Biol.*, 2014, **34**, 1445-1448.
26. A. Zeb, D. A. Hall, Z. Aslam, J. Forrester, J.-F. Li, Y. Li, C. C. Tang, G. Wang, F. Zhu and S. J. Milne, *Acta Mater.*, 2019, **168**, 100-108.
27. M. Otonicar, A. Reichmann and K. Reichmann, *J. Exp. Biol.*, 2016, **36**, 2495-2504.
28. W. Liu, T. Zheng, X. Ruan, Z. Man, H. Xue, L. Jiang, F. Zhang, G. Li and J. Wu, *J. Mater. Sci. Technol.*, 2023, **137**, 1-7.
29. P. Jaita, P. Jarupoom, R. Yimnirun, G. Rujijanagul and D. P. Cann, *Ceram. Int.*, 2016, **42**, 15940-15949.
30. Y. Zhang, H. Liu, S. Sun, Y. Liu, C. Huo, H. Qi, S. Deng and J. Chen, *ACS Appl. Mater. Interfaces.*, 2022, **14**, 13528-13538.
31. H. Tang, S. Zhang, Y. Feng, F. Li, T. R. Shrout and D. Johnson, *J. Am. Ceram. Soc.*, 2013, **96**, 2857-2863.
32. A. A. Bokov and Z. G. Ye, J. *Mater. Sci.*, 2006, **41**, 31-52.
33. R. A. Cowley, S. N. Gvasaliya, S. G. Lushnikov, B. Roessli and G. M. Rotaru, *Adv. Phys.*, 2011, **60**, 229-327.
34. F. Li, S. Zhang, D. Damjanovic, L.-Q. Chen and T. R. Shrout, *Adv. Funct. Mater.*, 2018, **28**, 1801504.
35. P. Wang, Q. Guo, F. Li, F. Xia, H. Hao, H. Sun, H. Liu and S. Zhang, *J. Am. Ceram. Soc.*, 2021,

104, 5127-5137.

36. R. E. Eitel, C. A. Randall, T. R. Shrout and S.-E. Park, *Jpn. J. Appl. Phys*, 2002, 41, 2099.
37. N. Wang, Y. Zhang, H. Luo, S. Sun, H. Liu and J. Chen, *J. Mater. Chem. C*, 2024, 12, 3345-3352.
38. H. Zhao, Y. Hou, X. Yu, M. Zheng and M. Zhu, *Acta Mater.*, 2019, **181**, 238-248.
39. M. Habib, M. H. Lee, F. Akram, M.-H. Kim, W.-J. Kim and T. K. Song, *J. Alloys Compd.*, 2021, **851**, 156788.
40. H. Luo, H. Liu, S. Deng, S. Hu, L. Wang, B. Gao, S. Sun, Y. Ren, L. Qiao and J. Chen, *Acta Mater.*, 2021, **208**, 116711.
41. Q. Guo, F. Li, F. Xia, P. Wang, X. Gao, H. Hao, H. Liu, H. Sun and S. Zhang, *J. Materiomics*, 2021, **7**, 683-692.
42. B. Gao, H. Qi, H. Liu and J. Chen, *Chin. Chem. Lett.*, 2024, **35**, 108598.
43. B. Gao, H. Liu, Z. Zhou, K. Xu, H. Qi, S. Deng, Y. Ren, J. Sun, H. Huang and J. Chen, *Microstructures*, 2022, **2**, 2022010.
44. N. Luo, S. Zhang, Q. Li, Q. Yan, W. He, Y. Zhang and T. R. Shrout, *Appl. Phys. Lett.*, 2014, **104**, 182911.
45. H. Liu, J. Chen, L. Fan, Y. Ren, L. Hu, F. Guo, J. Deng and X. Xing, *Chem. Mater.*, 2017, **29**, 5767-5771.
46. L. Fan, J. Chen, Y. Ren, Z. Pan, L. Zhang and X. Xing, *Phys. Rev. Lett.*, 2016, **116**, 027601.
47. Y. Zhang, H. Qi, S. Sun, Y. Liu, B. Gao, L. Wang, C. Huo, Y. Ren, S. Deng, H. Liu and J. Chen, *Nano Energy,* 2022, **104**, 107910.
48. Y. Liu, J. Yang, S. Deng, Y. Zhang, Y. Zhang, S. Sun, L. Wang, X. Jiang, C. Huo, H. Liu, H. Qi, S. Liu and J. Chen, *Acta Mater.,* 2022, **236**, 118115

Data Availability Statement

Data available on request from the authors.